Long-distance coherent propagation of magnon polarons in a ferroelectric-ferromagnetic heterostructure

Hanchen Wang,[1,2,3,*] Yuben Yang,[4,*] Jilei Chen,[2,5,*] Jinlong Wang,[1,*] Hao Jia,[2,5] Peng Chen,[6] Yuelin Zhang,[1] Caihua Wan,[6] Song Liu,[2,5] Dapeng Yu,[2,5] Xiufeng Han,[6] Jean-Philippe Ansermet,[7,†] Jinxing Zhang,[4,‡] and Haiming Yu[1,2,§]

[1]*Fert Beijing Institute, MIIT Key Laboratory of Spintronics, School of Integrated Circuit Science and Engineering, Beihang University, Beijing 100191, China*

[2]*International Quantum Academy, Shenzhen 518048, China*

[3]*Department of Materials, ETH Zurich, Zurich 8093, Switzerland*

[4]*Department of Physics, Beijing Normal University, Beijing 100875, China*

[5]*Shenzhen Institute for Quantum Science and Engineering, Southern University of Science and Technology, Shenzhen 518055, China*

[6]*Beijing National Laboratory for Condensed Matter Physics, Institute of Physics, University of Chinese Academy of Sciences, Chinese Academy of Sciences, Beijing 100190, China*

[7]*Institute of Physics, École Polytechnique Fédérale de Lausanne (EPFL), 1015 Lausanne, Switzerland*

(Received 9 August 2023; revised 26 September 2023; accepted 9 October 2023; published 20 October 2023)

We experimentally demonstrate the coherent propagation of magnon polarons, the hybridized excitations formed by the coupling of spin waves and Rayleigh/Love surface acoustic waves, in a heterostructure consisting of ferroelectric $BaTiO_3$ and ferromagnetic $La_{0.67}Sr_{0.33}MnO_3$. By systematically adjusting external magnetic field strengths and angles with respect to the wave vector, the wavelengths of coherent magnon polarons can be precisely controlled and maintained over distances of up to 80 μm. Their excitation was obtained using nanoscale interdigital transducer antennas. Our theoretical model, based on effective interlayer magnetoelastic coupling, reproduces the experimental transmission spectra, in particular the anticrossing features, allowing us to estimate the magnetoelastic coupling strength in this system to be of the order of 2×10^5 J/m^3. Our findings provide valuable insights into the coherent properties of magnon polarons and open up possibilities for the design of functional devices in the fields of spintronics and magnonics.

DOI: 10.1103/PhysRevB.108.144425

I. INTRODUCTION

Hybrid magnonics, involving the interaction between magnons and other fundamental excitations, has experienced rapid growth and diversification in the past decade [1–9]. One of the objectives is to harness the favorable properties of other media excitations and integrate them with magnons, such as decay length or lifetime [10–14]. Magnons, quanta of spin waves, are being considered as a potential solution to address the energy consumption bottleneck, Joule heating, associated with traditional transistor technologies [15–27]. One particularly promising variant is the hybridization between spin waves and surface acoustic waves (SAWs), known as magnon polarons [14,28–46]. This approach holds great potential due to the widespread utilization of SAWs in various modern technologies, including the rf bandpass filters found in cell phones [47,48]. The combination of the unique properties of magnons with well-established SAW technology has led to the development of various nonreciprocal transmission devices, based on different magnetic systems that incorporate interfacial Dzyaloshinskii-Moriya interaction (iDMI) and interlayer interactions [49–60]. This innovative approach holds significant potential for technological applications, including the realization of magnetoacoustic isolators and circulators [61,62]. However, previous works predominantly relied on bulk piezoelectric materials and microscale interdigital transducers (IDT) antennas which excite a narrow wave vector range [63,64]. This limited the coherent coupling of magnon polarons due to the small wave vector value dictated by the large-scale IDT antenna. The bulk SAWs waveguide imposes restrictions on the precise control and manipulation of magnon polarons at the nanoscale, as well as the exploration of a broader range of suitable materials for SAWs. In addition, the phase-coherent propagation of the magnon polarons excited by IDT antennas has not been reported yet, which would hold the potential to pave the way for the creation of innovative acoustomagnonic device architectures.

In this paper, we present our findings on the coherent hybridization between Rayleigh/Love SAWs in ultrathin $BaTiO_3$ (BTO) thin film, a ferroelectric (piezoelectric) material, and spin waves in 20-nm-thick ferromagnetic $La_{0.67}Sr_{0.33}MnO_3$ (LSMO) thin films. Through magnetic hysteresis measurements under different field directions, we confirm the in-plane uniaxial anisotropy of the LSMO film. Using nanoscale interdigital transducer antennas, we achieve simultaneous

*These authors contributed equally to this work.
†jean-philippe.ansermet@epfl.ch
‡jxzhang@bnu.edu.cn
§haiming.yu@buaa.edu.cn

excitation and detection of coherent Rayleigh and Love surface acoustic waves in a 10-nm-thick BTO film, allowing for the extraction of their velocities from various distance-dependent devices. Upon introducing an external magnetic field, we observe coherent hybridization and anticrossing between spin waves and Rayleigh/Love surface acoustic waves in the transmission spectra. Furthermore, by appropriately adjusting the field strength and angle with respect to the wave vector, we can precisely manipulate the wavelength of coherent magnon polarons, which can be calculated using a two-mode dispersion model. We attribute the coupling mechanism to an effective interlayer magnetoelastic coupling and develop a theoretical model that reproduces the experimental results. We estimate the coupling strength in our sample to be approximately 2×10^5 J/m^3. Our findings provide perspective on the electric field manipulation of coherent magnon polarons and the potential for long-distance guiding of these hybridized excitations using ferroelectric polarization patterns in ferroelectric/ferromagnetic heterostructures.

II. SAMPLE AND EXPERIMENT

The $BaTiO_3/La_{0.67}Sr_{0.33}MnO_3$ (BTO/LSMO) heterostructure was grown on $NdGaO_3$ (NGO) (110) oriented substrate by pulsed laser deposition using a KrF excimer laser (wavelength 248 nm) at a frequency of 5 Hz. During the growth of 20-nm-thick LSMO, the substrate temperature was maintained at 780 °C, oxygen pressure was kept at 25.0 Pa, and laser fluence was about 0.7 J/cm^2. Subsequently, a 10-nm-thick BTO film was grown at a substrate temperature of 730 °C and an oxygen pressure of 2.0 Pa. After the growth of the heterostructure, the whole film was slowly cooled down to room temperature at 5.0 °C/min under an oxygen pressure of 10^4 Pa. More information about the crystal information and ferroelectric property of the BTO layer can be found in Appendix A. It is worth noting that the different a and b axes lattice constants of the NGO substrate impose different strains to the LSMO thin film, inducing an in-plane uniaxial magnetic anisotropy in it. Magnetic hysteresis loops [Fig. 1(c)] with applying external magnetic fields in different in-plane directions show that the easy axis of the LSMO is [100] and the hard axis is [010] [65].

Subsequently, nanoscale IDT antennas consisting of three pairs of nanostripe lines were fabricated using e-beam lithography, e-beam evaporation, and liftoff processes. To achieve sufficiently large wave vector values for the coupling between spin waves in LSMO and surface acoustic waves in BTO, the antennas' width w is set at 200 nm, with a 200 nm gap between each wire. In other words, the periodicity a in Fig. 1(a) is 400 nm. The antennas are oriented so that the wave vector direction aligns with the hard axis of LSMO, i.e., in the [010] direction. The IDT antennas consist of a 10-nm-thick Ti layer and a 120-nm-thick gold layer. The electrodes of the antennas are connected to a vector network analyzer (VNA) using microwave probes. To excite SAWs through the piezoelectric effect of BTO, voltages with microwave frequency are applied to the excitation IDT antenna 1 (2). After propagating a distance s, the detection IDT antenna 2 (1) captures the signal through the inverse process. The power level for all

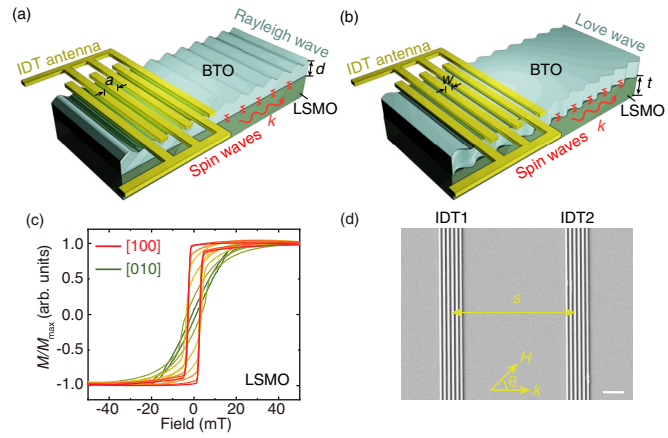

FIG. 1. (a),(b) Diagram illustrating the excitation of Rayleigh and Love surface acoustic waves in a BTO thin film using an IDT antenna, where zigzags represent the coupling of the SAW in BTO with spin waves in LSMO. (c) Magnetic hysteresis loops of the heterostructure under the application of an external magnetic field along the in-plane easy [100] (red curve) and hard [010] axes (green curve). The loops are measured at various angles with a step of 15°, revealing the magnetic anisotropy of the system. (d) Scanning electron microscopy (SEM) image of the nano-IDT antennas used for excitation and detection. The separation distance between the two antennas is denoted as s and the scale bar represents a length of 2 μm.

measurements in this work is fixed at 0 dBm. All the IDT devices used in the following sections have their wave vectors aligned along the [010] crystalline orientation of the BTO thin film, unless specified otherwise. All the transmission spectra shown in the following section are the imaginary part of the microwave scattering matrix S_{12} or S_{21}. Additionally, the terms Damon-Eshbach (DE) and backward volume (BV) will be employed in the upcoming sections to clarify the orientations between the wave vector of the antenna and external field directions (0° for BV; 90° for DE).

III. RESULTS AND DISCUSSION

In our study, the BTO thin film has a thickness of only 10 nm, making it challenging to identify whether the observed acoustic waves in our experiments are surface modes or quasibulk modes in BTO. In the following, we refer to the observed waves as the longitudinal acoustic (LA) mode for the Rayleigh acoustic wave, which propagates in the longitudinal direction relative to the wave vector k, and the transverse acoustic (TA) mode for the Love acoustic wave, which propagates in the transverse direction relative to the wave vector k.

The SAWs velocities of LA and TA modes can be determined by measuring a series of devices with different propagation distances. Figure 2(a) illustrates the imaginary part of the transmission spectra on different devices, exhibiting distinct phase oscillations between 2.8 and 5.5 GHz. These oscillations manifest as two envelopes with varying amplitudes, corresponding to the coherent propagation signals of the TA and LA modes. We assign the low frequency

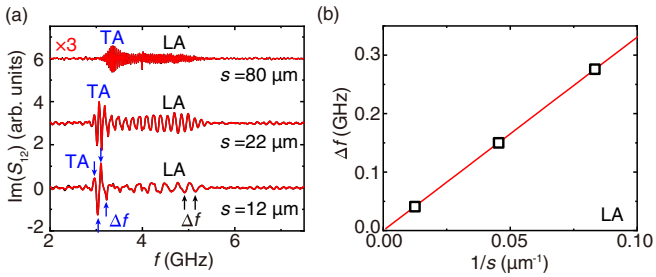

FIG. 2. (a) Surface acoustic waves transmission spectra obtained at different propagation distances in the absence of a magnetic field. Two distinct envelopes of oscillations corresponding to the TA and LA modes are observed. (b) Frequency differences between two neighboring peaks as a function of the inverse of the propagation distance when the frequency is around 5 GHz.

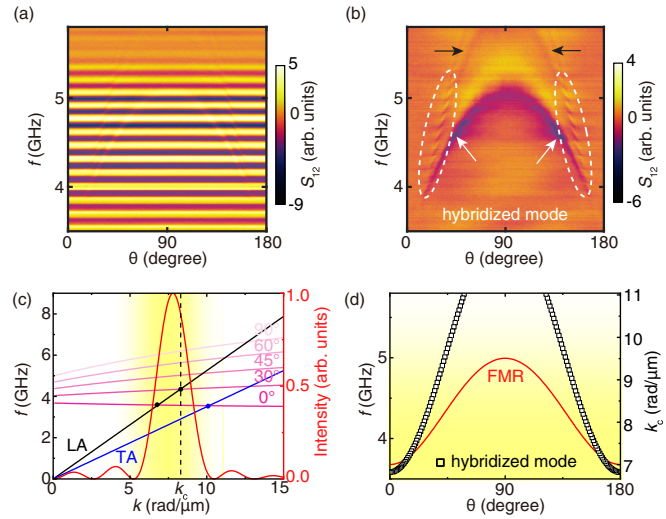

FIG. 3. (a) Angle (θ)-dependent transmission spectra of SAWs at 50 mT, where the acoustic mode remains unaffected by the external magnetic field. (b) Same data after subtracting the acoustic wave mode at 0°, where the white arrows and dashed windows indicate the hybridized modes and black arrows indicate the incoherent hybridized modes. (c) Dispersion of the LA, TA modes, and spin waves at different angles between the wave vector k and the external magnetic field $\mu_0 H$ [Eqs. (2) and (4)]. Yellow background: the wave vector distribution of the nano-IDT antenna (the red curve and the right y axis). (d) Theoretical predictions of the angle-dependent FMR and hybridized modes at 50 mT. The right y axis corresponds to the calculated wave vector values relative to their respective frequencies (left y axis).

envelope to TA and the high frequency envelope to LA modes due to their relative velocities [36]. Notably, the amplitude of the TA mode is approximately twice as large as that of the LA mode. In devices with greater propagation distances s, the transmission amplitudes decrease and the frequency differences between neighboring peaks (indicated by black arrows) reduce. Considering the phase difference between two neighboring peaks is 2π, the velocities of the LA and TA modes can be determined using the following equation [66–68]:

$$v_{\mathrm{SAW}} = \frac{\omega}{k} \approx \frac{2\pi\,\Delta f}{\Delta k} = \frac{2\pi\,\Delta f}{2\pi/s} = s\Delta f, \tag{1}$$

where s is the propagation distance. Assuming a fixed center frequency between two neighboring peaks, the frequency differences Δf are expected to be inversely proportional to s. To mitigate the influence of the overlapping frequency range between the LA and TA modes, we select the frequency differences at 5 GHz from various devices. By conducting linear fitting on Fig. 2(b), the velocity of the LA mode is estimated to be approximately 3.3 km/s, which has also been further verified by time-domain measurement. In order to check whether the piezoelectric properties of BTO are anisotropic, we also estimated the LA mode speed when the wave vector k direction is along [100] crystalline orientation of the BTO thin film, which is found about 3.0 km/s. The detailed information about time-domain and crystalline-dependent measurements can be found in Appendix B. Both these estimated values of the LA mode speeds are comparable to the previous values about 3.0 km/s reported in bulk BTO materials [69,70]. The deviation of the speed between the bulk and our sample can be reasonable due to the small thickness of the BTO thin film as compared to the acoustic wavelength and the strains imposed by substrates. However, obtaining an accurate velocity value for the TA mode is challenging due to the overlap with the LA mode. Nonetheless, based on the device with $s = 12$ μm (blue arrows), where the TA mode is more prominent than the LA mode, an estimated velocity range from approximately 1.7 to 2.3 km/s can be inferred for the TA mode. Based on the aforementioned experimental results, we find that both the LA and TA modes can coherently propagate over 80 μm, although the thickness of the BTO thin film is only 10 nm. This demonstrates the excellent performance of the BTO thin film in generating and propagating SAWs with efficient elastic-electric coupling. In the subsequent part of our study, we introduce an in-plane external magnetic field to tune the intrinsic spin wave frequencies in the adjacent LSMO thin film, aiming to explore the interlayer magnon-phonon coupling. As depicted in Fig. 3(a), we maintain a fixed external magnetic field strength of 50 mT and record the angle-dependent transmission spectra without subtracting any reference spectrum. Notably, we observe distinct and consistent phase oscillations in the spectra under 5.3 GHz at any magnetic field strengths. These phase oscillations correspond to the coherent propagation of the LA mode. Upon closer examination of the LA mode oscillations, it becomes evident that two distinct modes emerge beneath it, with one of them inducing anticrossing or distortions in the LA mode. These two modes become more apparent in Fig. 3(b) when we eliminate the coherent transmission signal of the LA mode by subtracting a reference spectrum recorded at 0°. At each angle, apart from the LSMO FMR mode, which exhibits strong intensity, an unexpected angle-dependent mode with higher frequency and phase oscillations becomes visible in the spectra (indicated by white dashed windows). To gain further insights into this feature, we extract magnetic parameters through the fitting of the FMR mode in Fig. 3(b). This, in combination with field-dependent reflection spectra at the easy and hard axes (see Appendix C),

is accomplished using the dispersion equation of dipole-exchange spin waves derived by Kalinikos and Slavin [71,72],

$$f_{\mathrm{SW}} = \frac{|\gamma|\mu_0}{2\pi}\left[\left(H_{\mathrm{ext}} + H_{\mathrm{easy}}\sin^2\phi - H_{\mathrm{hard}}\cos^2\phi + \frac{2A}{\mu_0 M_{\mathrm{s}}}k^2\right)\left(H_{\mathrm{ext}} + H_{\mathrm{easy}}\sin^2\phi - H_{\mathrm{hard}}\cos^2\phi + \frac{2A}{\mu_0 M_{\mathrm{s}}}k^2 + FM_{\mathrm{s}}\right)\right]^{\frac{1}{2}}, \quad (2)$$

$$F = 1 - \left(1 - \frac{1-e^{-kt}}{kt}\right)\cos^2\theta + \left(\frac{M_{\mathrm{s}}}{H_{\mathrm{ext}} + H_{\mathrm{easy}}\sin^2\phi - H_{\mathrm{hard}}\cos^2\phi + \frac{2A}{\mu_0 M_{\mathrm{s}}}k^2}\right)\left(\frac{1-e^{-2kt}}{4}\right)\sin^2\theta, \quad (3)$$

where θ is the angle between wave vector k and external magnetic field $\mu_0 H_{\mathrm{ext}}$, ϕ is the angle between external magnetic field and hard axis, and $t = 20$ nm is the thickness of the LSMO thin film. In our work, the wave vector of the antenna is parallel to the hard axis of the LSMO thin film, namely, $\phi = \theta$. The fitting results yield a saturation magnetization $\mu_0 M_{\mathrm{s}}$ of approximately 490 mT. Furthermore, the anisotropy fields along the easy and hard axes are determined to be around 8 mT and 17 mT, respectively. In Fig. 3(d), we present the theoretical reproduction of the angle-dependent FMR and the hybridized mode frequencies (shown as the red curve), which we explain in detail later.

We then proceed to analyze the observed magnon-phonon hybridized mode in the wave vector space. By utilizing the dimensions of the IDT antenna obtained from the SEM image, the wave vector distribution is calculated using fast Fourier transformation [Fig. 3(c)]. The plot reveals a finite wave vector window with maximum intensity occurring at 7.85 rad/μm. This result confirms that the antennas are specifically designed and sensitive to excite and detect coherent propagating waves within this particular wave vector range, which is corroborated by the coherence of the LA mode shown in Fig. 3(a). The frequency of the LA mode can be expressed as follows:

$$2\pi f_{\mathrm{SAW}} = v_{\mathrm{SAW}} k, \quad (4)$$

where the v_{SAW} for LA mode is 3.3 km/s. The wave vector distribution of the IDT antenna reveals a window ranging from 5 to 10 rad/μm. Using Eq. (4), we determine that the corresponding frequency range of the LA mode is from 2.6 to 5.3 GHz, consistent with the absence of phase oscillations in Fig. 3(a) beyond 5.3 GHz. To provide a visual aid, we have included yellow color-coded backgrounds in Figs. 3(c) and 3(d). The hybridized mode observed in Fig. 3(b) is a result of the crossing between the magnon and phonon dispersions. By fitting the crossing frequencies at different angles, we estimate the exchange stiffness constant A of the LSMO to be approximately 0.1374×10^{-16} m^2, which is consistent with Refs. [32,73]. For instance, at an angle of 30° between k and $\mu_0 H_{\mathrm{ext}}$, the crossing wave vector k_c between the magnon and LA phonon occurs at 8.28 rad/μm, falling within the antenna sensitive window. However, due to the lower speed of the TA phonon, at the same angle, the crossing wave vector between the magnon and TA phonon is much larger, approximately 12.8 rad/μm, which cannot be observed using the present design of the IDT antenna. Moreover, as the external magnetic field rotates from 0 (BV mode) to 90° (DE mode), both the crossing wave vector and frequency increase, as calculated using Eqs. (2) and (4). These calculated results are plotted as black squares in Fig. 3(d). The data are reported in frequency (left y axis) and in crossing wave vector k (right y axis). Beyond 5.3 GHz, the coherent hybridized mode [indicated by white windows in Fig. 3(b)] disappears in the experimental results due to a wave vector out of the excitation range of the antenna. However, an incoherent hybridized mode without phase oscillations can still be observed, indicating an incoherent hybridized scenario which happens in vicinity to the crossing wave vector point [black arrows in Fig. 3(b)], as previously reported [12]. It is worth noting that the incoherent hybridization means that the excited wave vector does not reach the required crossing wave vector of two mode dispersion but locates around the anticrossing gap, and the phase information or group velocity of the incoherent hybridized mode cannot be clearly observed from experimental transmission spectra. However, in this case, there is still some intermixing of the two physical subsystems. Furthermore, when the angle between the external magnetic field and the wave vector is fixed, performing field-dependent measurements allows us to clearly observe the hybridized mode in the transmission spectra. For instance, at 30°, the hybridization between the spin waves in LSMO and the LA mode in BTO induces significant distortions in the phase oscillations of the coherent LA mode, as depicted in Fig. 4(a). By subtracting a reference spectrum at −80 mT, it becomes evident that the

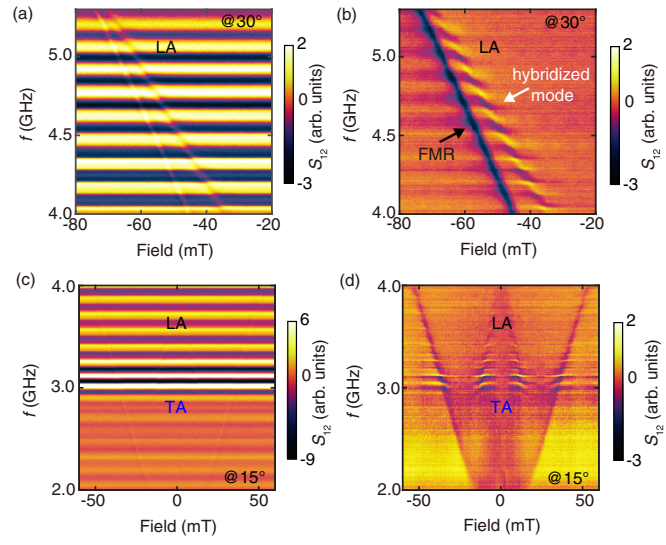

FIG. 4. (a) Field-dependent transmission spectra at $\theta = 30°$. (b) Same data after subtracting the field-independent acoustic wave signal, revealing two distinct modes. (c) Field-dependent transmission spectra at $\theta = 15°$, showing the coexistence of the LA and TA (stronger) modes. (d) Hybridized spin waves and TA modes after subtracting the field-independent acoustic wave signal.

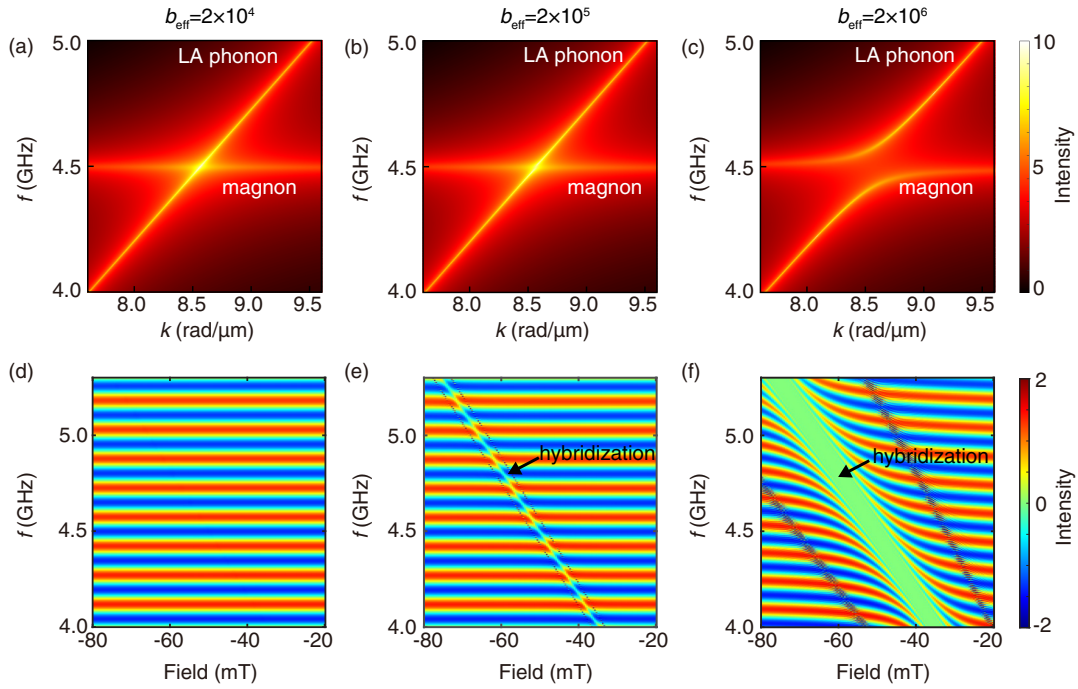

FIG. 5. (a)–(c) Hybridized dispersion of spin waves and LA mode calculated using Eq. (5) when the angle is 30° at −50 mT with $b_{\text{eff}} = 2\times10^4$ J/m^3, 2×10^5 J/m^3, and 2×10^6 J/m^3, respectively. (d)–(f) Calculated transmission spectra at 30°, corresponding to (a)–(c).

hybridized mode approaches the FMR mode as the external magnetic field strength increases. Based on the relationship between the frequency and wavelength of the LA mode, we can confidently state that the crossing wave vector between the magnon and phonon is enhanced at larger field strengths, while the frequency difference between the FMR and hybridized mode diminishes. This observation suggests that the dispersion of the magnon component becomes flatter compared to that at lower fields, which is influenced by dipolar interactions. The field-dependent transmission spectra and the features of the hybridized mode measured at different angles can be found in Appendix D. We also found that the low-velocity TA mode can hybridize with the propagating spin waves in LSMO. As illustrated in Figs. 4(c) and 4(d), after subtracting the phase oscillation of the TA and LA modes, a distinct anticrossing between the TA mode and the spin wave resonance mode is observed at 15°, which is near the BV configuration. In this configuration, the spin-wave dispersion is nearly flat in the dipole-exchange regime, allowing for crossing with the TA mode within the allowed wave vector window through tuning of the external magnetic field strength. Upon closer inspection of Fig. 4(d), it appears that the FMR mode directly couples with the TA mode. This is because the spin wave dispersion is flat and spin waves with different wavelengths are nearly degenerated around a single frequency. The observed coherent magnon polarons can propagate up to 80 μm and further details can be found in Appendix E.

To gain further insight into the experimentally observed hybridized features, we employ a theoretical model that takes into account the interaction between spin waves in LSMO and the LA mode in BTO. In accordance with the previous theoretical model, we introduce an effective magnetoelastic coupling strength b_{eff} to simulate the coupling between surface acoustic waves (SAWs) and spin waves. The eigenfrequencies of the hybridized mode dispersion can be expressed as follows [12,32,74]:

$$\omega^2 = \frac{\left(v_{\text{SAW}}^2 k^2 M_S^2 + \gamma^2 F_{\parallel} F_{zz}\right)}{2M_S^2} \pm \sqrt{\frac{\left(v_{\text{SAW}}^2 k^2 M_S^2 - \gamma^2 F_{\parallel} F_{zz}\right)}{2M_S^2} + \frac{4\gamma^2 F_{zz}|k|^3 t b_{\text{eff}}}{\rho M_S^2}}, \tag{5}$$

where ρ is the mass density, M_S is the saturation magnetization of LSMO, and $F_{\parallel} = \mu_0 M_S H_{\text{ext}} + \mu_0 M_S^2[1 - (1 - e^{-kt})/kt] + Ak^2 - K\cos 2\theta$ and $F_{zz} = \mu_0 M_S H_{\text{ext}} + \mu_0 M_S^2(1 - e^{-kt})/kt + Ak^2 - K\sin^2\theta$, with A the exchange constant and K the uniaxial magnetic anisotropy. In order to reproduce the experimentally observed transmission spectra in the view of SAWs propagation [Fig. 4(a)], we fixed the angle θ at 30° and varied the effective magnetoelastic coupling strength b_{eff}. The results of the hybridized dispersion and simulated transmission spectra for three different b_{eff} values are presented in Fig. 5. For $b_{\text{eff}} = 2\times10^4$ J/m^3, the resulting hybridized mode (distortions of the LA mode) in the transmission spectra is not prominent enough to generate a clear anticrossing gap [Fig. 5(a)] or noticeable distortions in the LA mode [Fig. 5(d)]. Increasing b_{eff} to 2×10^5 J/m^3 leads to a clearer hybridized mode in the transmission spectra [black arrow in Fig. 5(e)], which closely resembles the experimental transmission spectra [Fig. 4(a)].

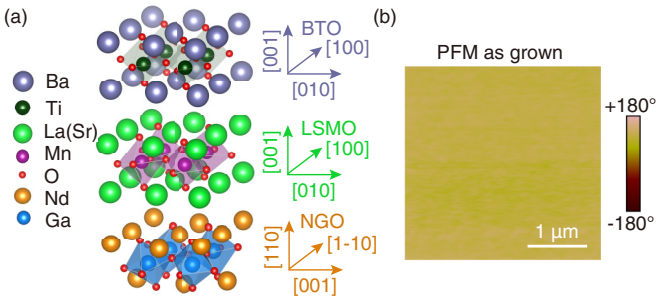

FIG. 6. (a) Schematic diagram of the crystal structure of BTO/LSMO/NGO, where the crystal orientation of BTO is [001], LSMO is [001], and NGO is [110] for the out-of-plane direction. (b) An as-grown out-of-plane ferroelectric polarization imaging measured by PFM on BTO/LSMO/NGO heterostructure, where the scale bar is 1 μm. The bright and dark contrasts indicate the downward and upward polarization states, respectively.

We also found that the anticrossing gap between magnon and LA phonon remains indistinct [Fig. 4(b)], indicating that the observed magnon polarons are in the weak coupling regime. It is worth noting that the ripples exhibiting narrower phase oscillation periodicity, observed near the hybridized mode under both larger and smaller magnetic fields, are artifacts or technical issues within our simulations. These patterns do not hold any physical significance or validity. A further increase in b_{eff} to 2×10^6 J/m^3 generates significant anticrossing gaps both in the hybridized dispersion and transmission spectra [Figs. 5(c) and 5(f)], indicating a strong coupling between the magnon and LA phonon. However, achieving this level of coupling strength in real devices is challenging at the current stage. Further theoretical and experimental investigations show great potential for achieving hybridized modes in the strong coupling regime. Several strategies merit consideration. First, in terms of materials, we can examine various ferroelectric materials with enhanced piezoelectric properties to determine their potential for enhancing interlayer magnetoelastic coupling when combined with LSMO. Second, from a physical standpoint, we can adjust the interlayer magnetoelastic coupling strength parameter through external forces and energy sources, such as electric fields applied to the BTO layer, ambient temperature modulation, or alterations in the thickness combinations between the LSMO and BTO layers.

IV. CONCLUSION

In conclusion, our experimental study demonstrates the generation and detection of coherent Rayleigh and Love surface acoustic waves in a 10-nm-thick BTO thin film using nanoscale IDT antennas. Through systematic manipulation of the external magnetic field strength and angle, we observe the coherent hybridization between acoustic waves and spin waves, which can propagate over distances of up to 80 μm. The wavelength of the magnon polarons can be precisely controlled by changing the external magnetic field strength. Our findings are well supported by a theoretical model based on effective interlayer magnetoelastic coupling, which reproduces the experimental observations and yields an estimated

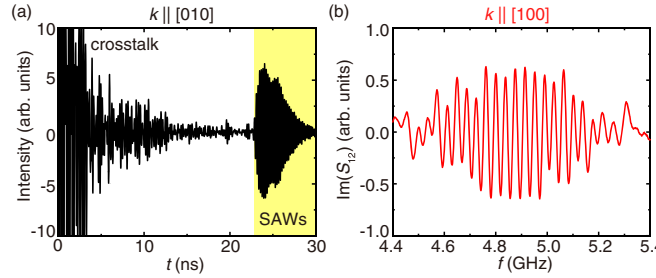

FIG. 7. (a) Time-domain measurement results on the device with wave vector pointing to the [010] crystalline orientation of the BTO layer without external magnetic field, where we can observe the SAWs-related signal from 23 ns to 30 ns. (b) An as-grown ferroelectric polarization imaging measured by PFM on BTO/LSMO/NGO heterostructure, where the scale bar is 1 μm.

coupling strength of the order of 2×10^5 J/m^3. Furthermore, the ferroelectric nature of the acoustic waveguide (BTO) opens up possibilities for electric field control, quantum acoustics [75], and the exploration of ferroelectric polarization patterns to guide coherent magnon polarons. These results lay the foundation for the development of functional devices based on coherent magnon polarons.

ACKNOWLEDGMENTS

We thank K. Yamamoto and S. Maekawa for helpful discussions. We thank R. Schlitz and W. Legrand for their constructive suggestions on this work. The authors acknowledge the support by the National Key Research and Development Program of China Grant No. 2022YFA1402801, NSF China under Grants No. 12074026 and No. U1801661, China Scholarship Council (CSC) under Grant No. 202206020091, and Shenzhen Institute for Quantum Science and Engineering, Southern University of Science and Technology (Grant No. SIQSE202007).

APPENDIX A: CRYSTAL STRUCTURE AND AS-GROWN FERROELECTRIC INFORMATION OF BTO/LSMO/NGO HETEROSTRUCTURE

In Fig. 6(a), we provide the detailed information about the crystal structure of the BTO/LSMO/NGO heterostructure. Pseudocubic (001)-orientation BTO and LSMO layers are

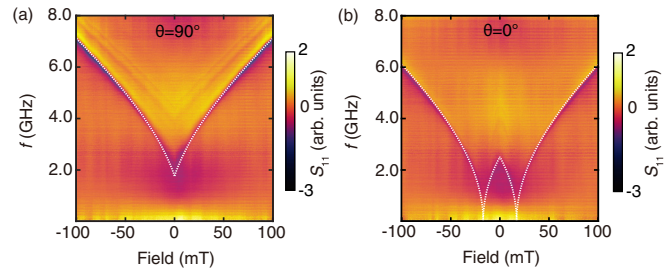

FIG. 8. (a),(b) Field-dependent reflection spectra measured with applying the external magnetic along easy ($\theta = 90°$) and hard ($\theta = 0°$) axes directions, where the dashed lines are the fitting by using Eqs. (2) and (3) with $k = 0$.

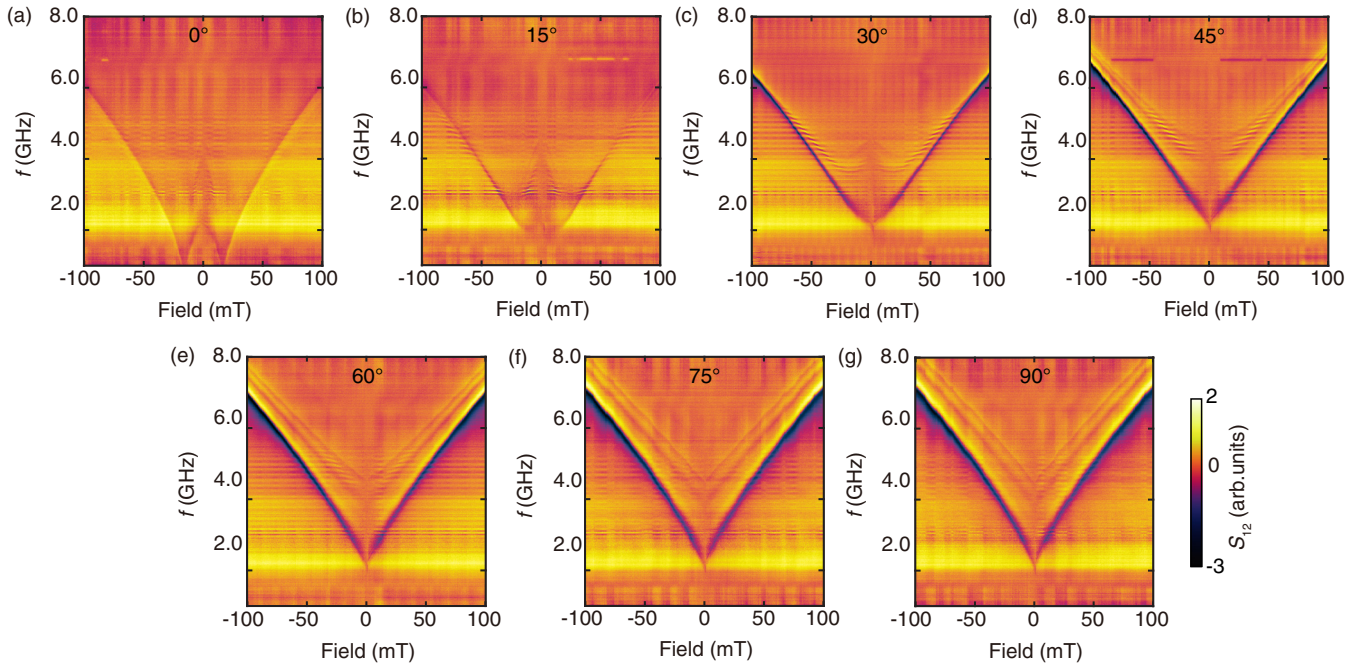

FIG. 9. (a)–(g) Transmission spectra measured on the device with propagation distance of 22 μm, which include the transition from BV to DE mode configuration. Field angle theta indicated at the top of each plot.

grown on the NGO substrate with (110) crystal plane orientation. After growth, we used the piezoelectric force microscopy (PFM) to check the ferroelectric property of the BTO layer. As shown in Fig. 6(b), the ferroelectricity in as-grown BTO on the top of LSMO presents a single domain scenario, indicating the simple ferroelectric and piezoelectric properties of the BTO layer to guide the SAWs. The PFM images were obtained using the scanning probe microscopy (Multimode 8 with controller V, Bruker) in off contact resonance mode with external lock-in amplifiers (SRS 830, Stanford Research Instruments). A Pt/Ir-coated tip on a Si cantilever (tip radius of 20 nm, force constant of 2.8 N/m, and a resonant frequency of 75 kHz) was used for characterizing the ferroelectricity. The amplitude and frequency of the actuating signal applied to the tip were 1 Vpp and 22 kHz, respectively (sample was grounded).

APPENDIX B: TIME-DOMAIN AND CRYSTALLINE-DEPENDENT MEASUREMENTS OF THE LA MODE VELOCITY

In Fig. 2, we extracted the velocities of the LA mode by a series of devices with different propagation distances. To further verify that the phase oscillations observed in the transmission spectra are indeed induced by the coherent SAWs propagation, we performed the time-domain measurements on the device with propagation distance of 80 μm whose wave vector is along [010] crystalline orientation as all the devices shown in Fig. 2. As shown in Fig. 7(a), a clear time difference can be observed due to the difference in propagation velocities for the LA acoustic mode and the electromagnetic waves ("crosstalk") traveling between the two IDT antennas. We found that the time window of the SAWs-related signal (yellow background) is from 23 ns to 30 ns, corresponding to a velocity value range from 3.5 to 2.7 km/s. The estimated value by using the transmission spectroscopy technique about 3.3 km/s is located within this value range given by the time-domain measurements, indicating that the transmission spectroscopy can provide more precise value of the SAWs velocity.

In addition, due to the anisotropic in-plane lattice constant of the NGO (110) substrate, the strains of the grown LSMO and BTO layers imposed by substrate will correspondingly have the anisotropic in-plane properties. For the LSMO layer, these anisotropic in-plane strains induce the easy and hard magnetic axes along [100] and [010] crystalline orientations. For the BTO layer, in order to check whether the piezoelectric properties are also in-plane anisotropic, we fabricated another same device with IDT antenna separated 80 μm while rotating the device 90° with respect to all the devices in Fig. 2 and the main text. Namely, the wave vector of the newly patterned IDT antennas are along the [100] direction of the BTO layer. Then, we choose to use the transmission spectroscopy to measure the SAWs' velocity, because it gives a more precise estimated value. The spectrum measured without an external magnetic field on the device is present in Fig. 7(b), from which we can only observe one envelope of the SAWs' signal that is attributed to the LA mode. By using Eq. (1), we realize that the velocity of the LA mode is about 3.0 km/s in the [100] direction, which is slightly smaller than the one in the [010] direction about 3.3 km/s.

APPENDIX C: FITTING OF THE FIELD-DEPENDENT FMR SPECTRA AT EASY AND HARD AXES

In Fig. 8, the reflection spectra measured under external magnetic fields along the easy and hard axes are fitted using Eqs. (2) and (3), with the wave vector (k) fixed at 0 rad/μm

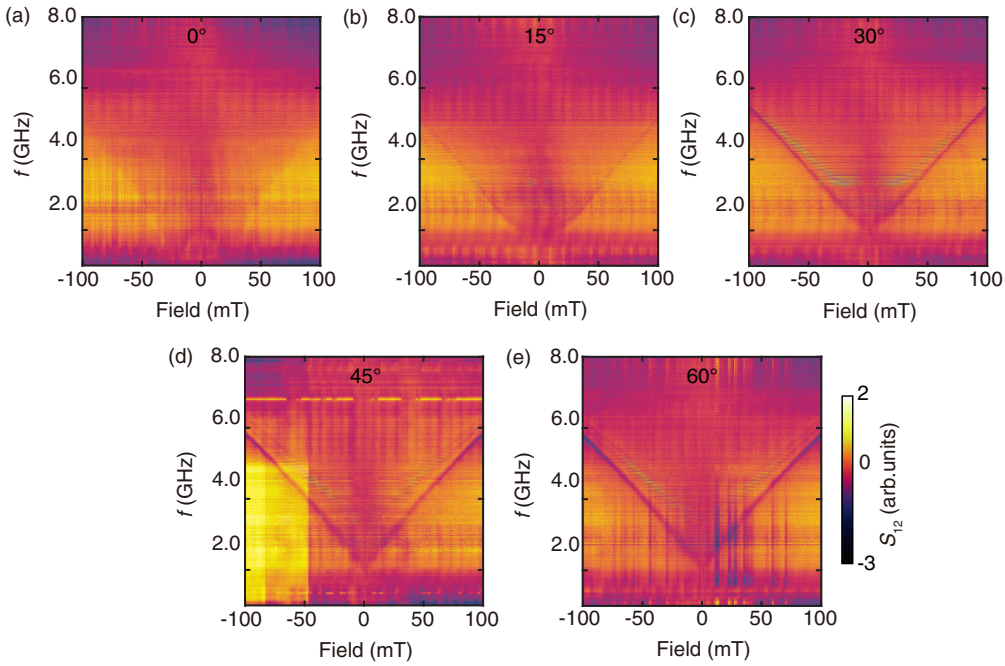

FIG. 10. (a)–(e) Transmission spectra measured on the device with propagation distance of 80 μm at different angles between field and wave vector. Field angle values indicated at the top of each plot.

(represented by the white dashed curves). By analyzing the fitting results, we extract the effective crystalline anisotropy field strengths along the easy and hard axes, as well as the saturation magnetization. These extracted parameters (saturation magnetization is about 490 mT; anisotropy field along easy and hard axes are around 8 and 17 mT) provide valuable insights for further fitting of dispersion and angle-dependent spectra.

APPENDIX D: MAGNON-POLARONS TRANSMISSION SPECTRA AT DIFFERENT FIELD DIRECTIONS

In Fig. 9, we present the transmission spectra measured at various external field directions between the easy and hard axes, complementing the data discussed (15° and 30°) in the main text. Based on the spectra provided in Fig. 9, the coherent magnon-polaron transmission signal is evident for angle ranges from 0° to 60°. Notably, the LA mode exhibits coupling between 15° and 60°, while the hybridization between the TA mode and magnons is observed only at 0° or 15° with lower field strengths. The absence of hybridization at angles above 60° is attributed to the inability of the IDT antennas to provide the required crossing wave vector in the dispersion. Furthermore, above the FMR mode, there are higher-order modes present, with the coherent magnon-polaron mode positioned at a lower frequency branch. Even though the coherent signal diminishes at higher frequencies due to limitations of the IDT antennas, we can still observe a mode without coherent phase oscillation. This can be attributed to incoherent magnon-phonon coupling, where the wave vector provided by the antenna does not precisely reach the crossing wave vector point, but hybridization still occurs in the vicinity of the anticrossing gap [12,32].

APPENDIX E: LONG DISTANCE MAGNON-POLARONS TRANSMISSION SPECTRA

In this section, we demonstrate the long-distance propagation properties of magnon polarons, which are enabled by the low damping and long decay length of the surface acoustic waves. As shown in Fig. 10, the transmission spectra measured on a device with the same antenna design but an 80 μm propagation distance reveal a clear coherent signal of the magnon polarons, even though the FMR signal is relatively weak. The denser phase oscillations observed in the spectra with increasing propagation distance are a result of a fixed velocity and a larger distance traveled. According to Eq. (1), this leads to a smaller frequency difference (Δf) between neighboring peaks.

[1] D. D. Awschalom, C. R. Du, R. He, F. J. Heremans, A. Hoffmann, J. Hou, H. Kurebayashi, Y. Li, L. Liu, V. Novosad *et al.*, Quantum engineering with hybrid magnonic systems and materials, IEEE Trans. Quantum Eng. **2**, 1 (2021).

[2] H. Y. Yuan, Y. Cao, A. Kamra, R. A. Duine, and P. Yan, Quantum magnonics: When magnon spintronics meets quantum information science, Phys. Rep. **965**, 1 (2022).

[3] B. Z. Rameshti, S. V. Kusminskiy, J. A. Haigh, K. Usami, D. Lachance-Quirion, Y. Nakamura, C.-M. Hu, H. X. Tang, G. E.

W. Bauer, and Y. M. Blanter, Cavity magnonics, Phys. Rep. **979**, 1 (2022).

[4] Y. Li, W. Zhang, V. Tyberkevych, W.-K. Kwok, A. Hoffmann, and V. Novosad, Hybrid magnonics: Physics, circuits, and applications for coherent information processing, J. Appl. Phys. **128**, 130902 (2020).

[5] A. Frisk Kockum, A. Miranowicz, S. De Liberato, S. Savasta, and F. Nori, Ultrastrong coupling between light and matter, Nat. Rev. Phys. **1**, 19 (2019).

[6] X. Zhang, C.-L. Zou, L. Jiang, and H. X. Tang, Cavity magnomechanics, Sci. Adv. **2**, e1501286 (2016).

[7] H. Huebl, C. W. Zollitsch, J. Lotze, F. Hocke, M. Greifenstein, A. Marx, R. Gross, and S. T. B. Goennenwein, High cooperativity in coupled microwave resonator ferrimagnetic insulator hybrids, Phys. Rev. Lett. **111**, 127003 (2013).

[8] X. Zhang, C.-L. Zou, L. Jiang, and H. X. Tang, Strongly coupled magnons and cavity microwave photons, Phys. Rev. Lett. **113**, 156401 (2014).

[9] L. Bai, M. Harder, Y. P. Chen, X. Fan, J. Q. Xiao, and C.-M. Hu, Spin pumping in electrodynamically coupled magnon-photon systems, Phys. Rev. Lett. **114**, 227201 (2015).

[10] H. Wang, W. He, R. Yuan, Y. Wang, J. Wang, Y. Zhang, I. Medlej, J. Chen, G. Yu, X. Han, J.-P. Ansermet, and H. Yu, Hybridized propagating spin waves in a CoFeB/IrMn bilayer, Phys. Rev. B **106**, 064410 (2022).

[11] Y. Tabuchi, S. Ishino, A. Noguchi, T. Ishikawa, R. Yamazaki, K. Usami, and Y. Nakamura, Coherent coupling between a ferromagnetic magnon and a superconducting qubit, Science **349**, 405 (2015).

[12] J. Zhang, M. Chen, J. Chen, K. Yamamoto, H. Wang, M. Hamdi, Y. Sun, K. Wagner, W. He, Y. Zhang *et al.*, Long decay length of magnon-polarons in $BiFeO_3/La_{0.67}Sr_{0.33}MnO_3$ heterostructures, Nat. Commun. **12**, 7258 (2021).

[13] J. Rao, C. Y. Wang, B. Yao, Z. J. Chen, K. X. Zhao, and W. Lu, Meterscale strong coupling between magnons and photons, Phys. Rev. Lett. **131**, 106702 (2023).

[14] K. An, A. N. Litvinenko, R. Kohno, A. A. Fuad, V. V. Naletov, L. Vila, U. Ebels, G. de Loubens, H. Hurdequint, N. Beaulieu, J. Ben Youssef, N. Vukadinovic, G. E. W. Bauer, A. N. Slavin, V. S. Tiberkevich, and O. Klein, Coherent long-range transfer of angular momentum between magnon Kittel modes by phonons, Phys. Rev. B **101**, 060407(R) (2020).

[15] M. Dabrowski, T. Nakano, D. M. Burn, A. Frisk, D. G. Newman, C. Klewe, Q. Li, M. Yang, P. Shafer, E. Arenholz, T. Hesjedal, G. van der Laan, Z. Q. Qiu, and R. J. Hicken, Coherent transfer of spin angular momentum by evanescent spin waves within antiferromagnetic NiO, Phys. Rev. Lett. **124**, 217201 (2020).

[16] A. V. Chumak, V. I. Vasyuchka, A. A. Serga, and B. Hillebrands, Magnon spintronics, Nat. Phys. **11**, 453 (2015).

[17] P. Pirro, V. I. Vasyuchka, A. A. Serga, and B. Hillebrands, Advances in coherent magnonics, Nat. Rev. Mater. **6**, 1114 (2021).

[18] V. Kruglyak, S. Demokritov, and D. Grundler, Magnonics, J. Phys. D **43**, 264001 (2010).

[19] A. Barman, G. Gubbiotti, S. Ladak, A. O. Adeyeye, M. Krawczyk, J. Gräfe, C. Adelmann, S. Cotofana, A. Naeemi, V. I. Vasyuchka *et al.*, The 2021 magnonics roadmap, J. Phys.: Condens. Matter **33**, 413001 (2021).

[20] L. J. Cornelissen, J. Liu, R. A. Duine, J. B. Youssef, and B. J. Van Wees, Long-distance transport of magnon spin information in a magnetic insulator at room temperature, Nat. Phys. **11**, 1022 (2015).

[21] R. Lebrun, A. Ross, S. A. Bender, A. Qaiumzadeh, L. Baldrati, J. Cramer, A. Brataas, R. A. Duine, and M. Kläui, Tunable long-distance spin transport in a crystalline antiferromagnetic iron oxide, Nature (London) **561**, 222 (2018).

[22] A. Serga, A. Chumak, and B. Hillebrands, YIG magnonics, J. Phys. D **43**, 264002 (2010).

[23] A. V. Chumak, P. Kabos, M. Wu, C. Abert, C. Adelmann, A. O. Adeyeye, J. Akerman, F. G. Aliev, A. Anane, A. Awad *et al.*, Advances in magnetics roadmap on spin-wave computing, IEEE Trans. Magn. **58**, 0800172 (2022).

[24] G. Csaba, A. Papp, and W. Porod, Perspectives of using spin waves for computing and signal processing, Phys. Lett. A **381**, 1471 (2016).

[25] V. Vlaminck and M. Bailleul, Current-induced spin-wave Doppler shift, Science **322**, 410 (2008).

[26] J. Han, P. Zhang, J. T. Hou, S. A. Siddiqui, and L. Liu, Mutual control of coherent spin waves and magnetic domain walls in a magnonic device, Science **366**, 1121 (2019).

[27] H. Merbouche, I. Boventer, V. Haspot, S. Fusil, V. Garcia, D. Gouéré, C. Carrétéro, A. Vecchiola, R. Lebrun, P. Bortolotti, L. Vila, M. Bibes, A. Barthelemy, and A. Anane, Voltage-controlled reconfigurable magnonic crystal at the sub-micrometer scale, ACS Nano **15**, 9775 (2021).

[28] F. Heyroth, C. Hauser, P. Trempler, P. Geyer, F. Syrowatka, R. Dreyer, S. G. Ebbinghaus, G. Woltersdorf, and G. Schmidt, Monocrystalline freestanding three-dimensional yttrium-iron-garnet magnon nanoresonators, Phys. Rev. Appl. **12**, 054031 (2019).

[29] M. Weiler, L. Dreher, C. Heeg, H. Huebl, R. Gross, M. S. Brandt, and S. T. B. Goennenwein, Elastically driven ferromagnetic resonance in nickel thin films, Phys. Rev. Lett. **106**, 117601 (2011).

[30] T. Kikkawa, K. Oyanagi, T. Hioki, M. Ishida, Z. Qiu, R. Ramos, Y. Hashimoto, and E. Saitoh, Composition-tunable magnon-polaron anomalies in spin Seebeck effects in epitaxial $Bi_xY_{3-x}Fe_5O_{12}$ films, Phys. Rev. Mater. **6**, 104402 (2022).

[31] J. Cui, E. Viñas Boström, M. Ozerov, F. Wu, Q. Jiang, J.-H. Chu, C. Li, F. Liu, X. Xu, A. Rubio, and Q. Zhang, Chirality selective magnon-phonon hybridization and magnon-induced chiral phonons in a layered zigzag antiferromagnet, Nat. Commun. **14**, 3396 (2023).

[32] J. Chen, K. Yamamoto, J. Zhang, J. Ma, H. Wang, Y. Sun, M. Chen, J. Ma, S. Liu, P. Gao, D. Yu, J.-P. Ansermet, C.-W. Nan, S. Maekawa, and H. Yu, Hybridized propagation of spin waves and surface acoustic waves in a multiferroic-ferromagnetic heterostructure, Phys. Rev. Appl. **19**, 024046 (2023).

[33] B. Casals, N. Statuto, M. Foerster, A. Hernández-Mínguez, R. Cichelero, P. Manshausen, A. Mandziak, L. Aballe, J. M. Hernández, and F. Maciá, Generation and imaging of magnetoacoustic waves over millimeter distances, Phys. Rev. Lett. **124**, 137202 (2020).

[34] C. Berk, M. Jaris, W. Yang, S. Dhuey, S. Cabrini, and H. Schmidt, Strongly coupled magnon-phonon dynamics in a single nanomagnet, Nat. Commun. **10**, 2652 (2019).

[35] H. Hayashi and K. Ando, Spin pumping driven by magnon polarons, Phys. Rev. Lett. **121**, 237202 (2018).
[36] T. Kikkawa, K. Shen, B. Flebus, R. A. Duine, K. I. Uchida, Z. Qiu, G. E.W. Bauer, and E. Saitoh, Magnon polarons in the spin Seebeck effect, Phys. Rev. Lett. **117**, 207203 (2016).
[37] J. Li, H. T. Simensen, D. Reitz, Q. Sun, W. Yuan, C. Li, Y. Tserkovnyak, A. Brataas, and J. Shi, Observation of magnon polarons in a uniaxial antiferromagnetic insulator, Phys. Rev. Lett. **125**, 217201 (2020).
[38] B. Zare Rameshti and R. A. Duine, Length scale for magnon-polaron formation from nonlocal spin transport, Phys. Rev. B **99**, 060402(R) (2019).
[39] M. Muller, J. Weber, F. Engelhardt, V. A. S. V. Bittencourt, T. Luschmann, M. Cherkasskii, S. T. B. Gönnenwein, S. V. Kusminskiy, S. Geprägs, R. Gross, M. Althammer, and H. Huebl, Chiral phonons and phononic birefringence in ferromagnetic metal-bulk acoustic resonator hybrids, arXiv:2303.08429.
[40] K. An, C. Kim, K.-W. Moon, R. Kohno, G. Olivetti, G. de Loubens, N. Vukadinovic, J. Ben Youssef, C. Hwang, and O. Klein, Optimizing the magnon-phonon cooperativity in planar geometries, Phys. Rev. Appl. **20**, 014046 (2023).
[41] M. Pomerantz, Excitation of spin-wave resonance by microwave phonons, Phys. Rev. Lett. **7**, 312 (1961).
[42] H. Matthews and R. C. LeCraw, Acoustic wave rotation by magnon-phonon interaction, Phys. Rev. Lett. **8**, 397 (1962).
[43] C. F. Kooi, Interaction of phonons and spin waves, Phys. Rev. **131**, 1070 (1963).
[44] P. M. Rowell, Microwave ultrasonics, Br. J. Appl. Phys. **14**, 60 (1963).
[45] C. F. Kooi, P. E. Wigen, M. R. Shanabarger, and J. V. Kerrigan, Spin-wave resonance in magnetic films on the basis of the surface-spin-pinning model and the volume inhomogeneity model, J. Appl. Phys. **35**, 791 (1964).
[46] P. E. Wigen, W. I. Dobrov, and M. R. Shanabarger, Coherent spin-wave-phonon interactions in thin magnetic films, Phys. Rev. **140**, A1827 (1965).
[47] S. Mahon, The 5G effect on rf filter technologies, IEEE Trans. Semicond. Manufact. **30**, 494 (2017).
[48] B. Dieny, I. L. Prejbeanu, K. Garello, P. Gambardella, P. Freitas, R. Lehndorff, W. Raberg, U. Ebels, S. O. Demokritov, J. Akerman *et al.*, Opportunities and challenges for spintronics in the microelectronics industry, Nat. Electron. **3**, 446 (2020).
[49] M. Xu, K. Yamamoto, J. Puebla, K. Baumgaertl, B. Rana, K. Miura, H. Takahashi, D. Grundler, S. Maekawa, and Y. Otani, Nonreciprocal surface acoustic wave propagation via magneto-rotation coupling, Sci. Adv. **6**, eabb1724 (2020).
[50] M. Kuss, M. Hassan, Y. Kunz, A. Hörner, M. Weiler, and M. Albrecht, Nonreciprocal magnetoacoustic waves in synthetic antiferromagnets with Dzyaloshinskii-Moriya, Phys. Rev. B **107**, 024424 (2023).
[51] M. Kuss, M. Hassan, Y. Kunz, A. Hörner, M. Weiler, and M. Albrecht, Nonreciprocal transmission of magnetoacoustic waves in compensated synthetic antiferromagnets, Phys. Rev. B **107**, 214412 (2023).
[52] M. Kuss, M. Heigl, L. Flacke, A. Hörner, M. Weiler, A. Wixforth, and M. Albrecht, Nonreciprocal magnetoacoustic waves in dipolar-coupled ferromagnetic bilayers, Phys. Rev. Appl. **15**, 034060 (2021).
[53] M. Kuss, M. Heigl, L. Flacke, A. Hörner, M. Weiler, M. Albrecht, and A. Wixforth, Nonreciprocal Dzyaloshinskii–Moriya magnetoacoustic waves, Phys. Rev. Lett. **125**, 217203 (2020).
[54] K. An, R. Kohno, A. N. Litvinenko, R. L. Seeger, V. V. Naletov, L. Vila, G. de Loubens, J. Ben Youssef, N. Vukadinovic, G. E. W. Bauer, A. N. Slavin, V. S. Tiberkevich, and O. Klein, Bright and dark states of two distant macrospins strongly coupled by phonons, Phys. Rev. X **12**, 011060 (2022).
[55] R. Schlitz, L. Siegl, T. Sato, W. Yu, G. E. W. Bauer, H. Huebl, and S. T. B. Goennenwein, Magnetization dynamics affected by phonon pumping, Phys. Rev. B **106**, 014407 (2022).
[56] C. Zhao, Y. Li, Z. Zhang, M. Vogel, J. E. Pearson, J. Wang, W. Zhang, V. Novosad, Q. Liu, and A. Hoffmann, Phonon transport controlled by ferromagnetic resonance, Phys. Rev. Appl. **13**, 054032 (2020).
[57] C. Cai, X.-H. Zhou, W. Yu, and T. Yu, Acoustic frequency multiplication and pure second-harmonic generation of phonons by magnetic transducers, Phys. Rev. B **107**, L100410 (2023).
[58] W. Yu, Dynamic exchange coupling between magnets mediated by attenuating elastic waves, Phys. Rev. B **108**, 134414 (2023).
[59] R. Verba, I. Lisenkov, I. Krivorotov, V. Tiberkevich, and A. Slavin, Nonreciprocal surface acoustic waves in multilayers with magnetoelastic and interfacial Dzyaloshinskii-Moriya interactions, Phys. Rev. Appl. **9**, 064014 (2018).
[60] P. J. Shah, D. A. Bas, I. Lisenkov, A. Matyushov, N. X. Sun, and M. R. Page, Giant nonreciprocity of surface acoustic waves enabled by the magnetoelastic interaction, Sci. Adv. **6**, eabc5648 (2020).
[61] C. E. Fay and R. L. Comstock, Operation of the ferrite junction circulator, IEEE Trans. Microwave Theory Techn. **13**, 15 (1965).
[62] J. D. Adam, L. E. Davis, G. F. Dionne, E. F. Schloemann, and S. N. Stitzer, Ferrite devices and materials, IEEE Trans. Microwave Theory Tech. **50**, 721 (2002).
[63] P. G. Gowtham, T. Moriyama, D. C. Ralph, and R. A. Buhrman, Traveling surface spin-wave resonance spectroscopy using surface acoustic waves, J. Appl. Phys. **118**, 233910 (2015).
[64] R. M. White and F. W. Voltmer, Direct piezoelectric coupling to surface elastic waves, Appl. Phys. Lett. **7**, 314 (1965).
[65] M. Wahler, B. Büttner, H.-H. Blaschek, N. Homonnay, O. Wid, K. J. O'Shea, D. McGrouther, D. A. MacLaren, and G. Schmidt, Controlling magnetic anisotropy in $La_{0.7}Sr_{0.3}MnO_3$ nanostructures, Appl. Phys. Lett. **104**, 052408 (2014).
[66] H. Yu, O. d'Allivy Kelly, V. Cros, R. Bernard, P. Bortolotti, A. Anane, F. Brandl, R. Huber, I. Stasinopoulos, and D. Grundler, Magnetic thin-film insulator with ultra-low spin wave damping for coherent nanomagnonics, Sci. Rep. **4**, 6848 (2014).
[67] H. Wang, J. Chen, T. Liu, J. Zhang, K. Baumgaertl, C. Guo, Y. Li, C. Liu, P. Che, S. Tu, S. Liu, P. Gao, X. Han, D. Yu, M. Wu, D. Grundler, and H. Yu, Chiral spin-wave velocities induced by all-garnet interfacial Dzyaloshinskii-Moriya interaction in ultrathin yttrium iron garnet films, Phys. Rev. Lett. **124**, 027203 (2020).
[68] H. Qin, S. J. Hamalainen, K. Arjas, J. Witteveen, and S. van Dijken, Propagating spin waves in nanometer-thick yttrium iron garnet films: Dependence on wave vector, magnetic field strength, and angle, Phys. Rev. B **98**, 224422 (2018).

[69] Yu. N. Gandurin and V. V. Kosachev, Reflection of surface acoustic waves in the bulk of a hexagonal single crystal, Phys. Solid State **56**, 373 (2014).

[70] S. Eskandari and H. M. Shodja, Shear horizontal surface acoustic waves in a magneto-electro-elastic system, J. Mech. Behav. Mater. **25**, 1 (2016).

[71] B. Kalinikos and A. Slavin, Theory of dipole-exchange spin wave spectrum for ferromagnetic films with mixed exchange boundary conditions, J. Phys. C: Solid State Phys. **19**, 7013 (1986).

[72] N. Zhu, H. Chang, A. Franson, T. Liu, X. Zhang, E. Johnston-Halperin, M. Wu, and H. X. Tang, Patterned growth of crystalline $Y_3Fe_5O_{12}$ nanostructures with engineered magnetic shape anisotropy, Appl. Phys. Lett. **110**, 252401 (2017).

[73] H. Wang, Y. Yang, M. Madami, Y. Wang, M. Du, J. Chen, Y. Zhang, L. Sheng, J. Zhang, C. Wen, Y. Zhang, S. Hao, G. Yu, X. Han, G. Gubbiotti, K. Shen, J. Zhang, and H. Yu, Anomalous anisotropic spin-wave propagation in thin manganite films with uniaxial magnetic anisotropy, Appl. Phys. Lett. **120**, 192402 (2022).

[74] K. Yamamoto, M. Xu, J. Puebla, Y. Otani, and S. Maekawa, Interaction between surface acoustic waves and spin waves in a ferromagnetic thin film, J. Magn. Magn. Mater. **545**, 168672 (2022).

[75] T. Luschmann, A. Jung, S. Geprägs, F. X. Haslbeck, A. Marx, S. Filipp, S. Gröblacher, R. Gross, and H. Huebl, Surface acoustic wave resonators on thin film piezoelectric substrates in the quantum regime, Mater. Quantum. Technol. **3**, 021001 (2023).